


Shell-model-like approach based on cranking covariant density functional theory to the antimagnetic rotation band in ^{101}Pd

Lang Liu (刘朗)*

*School of Science, Jiangnan University, Wuxi 214122, China
and State Key Laboratory of Nuclear Physics and Technology, School of Physics,
Peking University, Beijing 100871, China*

 (Received 2 November 2018; revised manuscript received 14 December 2018; published 21 February 2019)

The antimagnetic rotation band $\nu h_{11/2}$ in ^{101}Pd is investigated using cranking covariant density functional theory with a shell-model-like approach to treating the pairing correlations, in which the particle number is conserved strictly and the blocking effects are taken into account exactly. Four sets of pairing strength are adopted in the present calculations. The tendencies of the experimental moments of inertia, $B(E2)$ values, and spins are well reproduced with suitable pairing strengths. The up-bending mechanism of the antimagnetic rotation (AMR) band $\nu h_{11/2}$ in ^{101}Pd is studied in terms of the component of the total angular momentum alignment and the occupation numbers around the Fermi surface. It can be found that the up-bending is mainly triggered by the proton $1g_{9/2}$ orbital. Moreover, the proton angular momentum alignment, which mainly comes from the rearrangement of proton occupations in $1g_{9/2}$ orbitals and the increasing components of $1g_{9/2}$, plays an important role in the two-shears-like mechanism.

DOI: [10.1103/PhysRevC.99.024317](https://doi.org/10.1103/PhysRevC.99.024317)

I. INTRODUCTION

Antimagnetic rotation (AMR) in nuclei, which was predicted by Frauendorf [1,2], is a novel phenomenon observed in weakly deformed or near-spherical nuclei [2]. In AMR bands, the properties of energy spectra and angular momentum are explained by the two-shears-like mechanism, i.e., simultaneous closing of the two valence neutrons (protons) towards the direction of the proton (neutron) angular momentum vector. After AMR was proposed, it attracted a wide range of interest from both theoretical and experimental nuclear physicists.

From the theoretical aspect, AMR has been investigated with simple models with clear geometric pictures, such as the classical particle rotor model [3]. It has also been studied by using the tilted axis cranking (TAC) model [4–6]. Based on the TAC model, many applications have been carried out within the framework of the microscopic-macroscopic model [7–9] and pairing plus quadrupole model [2,10]. In particular, due to the great success of the covariant density functional theory (CDFT) in describing of ground states as well as excited states of nuclei throughout the nuclear chart [11–14], the TAC model has been combined with the CDFT for the study of AMR [15–18]. Subsequently, the TAC model with the point-coupling density functional theory [19] (TAC-CDFT) was developed and applied successfully to describe many phenomena, such as magnetic and chiral rotation [20], nuclear rod shape [21], etc. The TAC-CDFT has also been extended to include pairing correlations in order to study the rotational nuclei [22]. However, in most of the literature,

the pairing correlations are either neglected or treated by the Bogoliubov formalism, where the particle number is not conserved strictly. The violation of the particle number can cause serious problems [23,24]. Actually, all cranked Hartree-Fock-Bogolyubov (HFB) calculations show an unphysical phase transition for angular momentum greater than a critical value due to the pairing collapse [25]. The remedy with the particle-number projection or the Lipkin-Nogami method can restore this broken symmetry. Previous research showed that, after the particle-number projection, the calculated rotational properties can be improved considerably compared with the cranking HFB calculations [26]. However, the complicated numerical techniques make it difficult to generalize these methods to the higher excited states [24].

In order to solve the problem of nonconservation of particle number and other questions that it caused, Zeng and his collaborators introduced the particle number conservation (PNC) method by solving the Hamiltonian directly in a truncated multiparticle configuration space [23,27]. The particle number is conserved and the blocking effects are taken into account exactly in this method. Then, the PNC scheme was extended into nonrelativistic mean field models [28] and the total-Routhian-surface method with the Woods-Saxon potential [29,30]. Recently, the PNC method based on the cranking Skyrme-Hartree-Fock model was developed [31]. This conserving method with the cranked shell model (PNC-CSM) has also been employed successfully for describing various phenomenon concerning the rotating nuclei, e.g., the odd-even differences in moments of inertia (MOIs) [32], the identical bands [33,34], the nuclear pairing phase transition [35], the rotational bands and high- K isomers in the rare-earth [36–39] and actinide nuclei [40–43], etc. Under the covariant

*liulang@jiangnan.edu.cn

framework, the PNC method has been combined with the relativistic mean field (RMF) approach, which is also known as the shell-model-like approach in RMF (RMF+SLAP) [44], to investigate the properties of Sn [45], C [46] isotopes, α -cluster structure in light nuclei [47,48], quantum fluctuation of particle number [49,50], and the thermodynamics of pairing transition in hot nuclei [51]. Very recently, SLAP based on cranking covariant density functional theory (CDFT-SLAP) was developed to study the band crossing and shape evolution in ^{60}Fe [52].

Meanwhile, the experimental exploration of AMR has been performed in ^{105}Cd [53], ^{106}Cd [7], ^{108}Cd [8,54], ^{110}Cd [55], and ^{107}Cd [56]. In addition, further investigation of AMR by lifetime measurements has also been done in ^{109}Cd [10], ^{100}Pd [9], ^{144}Dy [57], and ^{112}In [58]. The high-spin states of ^{101}Pd have been studied experimentally in Ref. [59]. Subsequently, lifetime measurements were performed for the ν $h_{11/2}$ band in ^{101}Pd [60], which confirmed the previous assumption of the AMR nature of this band [59]. Very recently, the two-shears-like mechanism for this AMR band was studied in detail with CSM-PNC method [61]. However, the AMR band in ^{101}Pd has not been investigated in the CDFT framework, it is interesting to investigate the two-shears-like mechanism and the effects of pairing with cranking CDFT-SLAP.

This paper is organized as follows. A brief introduction to the cranking CDFT-SLAP theoretical framework is presented in Sec. II. In Sec. III, the numerical details of the calculation are presented. The results and discussion are given in Sec. IV. A brief summary is given in Sec. V.

II. THEORETICAL FRAMEWORK

In this section, a brief theoretical framework of CDFT-SLAP is given. More details about CDFT can be found in Refs. [11–14,19]. For CDFT-SLAP formalism, the literature [44,52] has detailed introductions. The starting point of the point-coupling CDFT is the effective Lagrangian density,

$$\begin{aligned} \mathcal{L} &= \mathcal{L}^{\text{free}} + \mathcal{L}^{4\text{f}} + \mathcal{L}^{\text{hot}} + \mathcal{L}^{\text{der}} + \mathcal{L}^{\text{em}} \\ &= \bar{\psi}(i\gamma_\mu \partial^\mu - m)\psi \\ &\quad - \frac{1}{2}\alpha_S(\bar{\psi}\psi)(\bar{\psi}\psi) - \frac{1}{2}\alpha_V(\bar{\psi}\gamma_\mu\psi)(\bar{\psi}\gamma^\mu\psi) \\ &\quad - \frac{1}{2}\alpha_{TV}(\bar{\psi}\vec{\tau}\gamma_\mu\psi)(\bar{\psi}\vec{\tau}\gamma^\mu\psi) \\ &\quad - \frac{1}{3}\beta_S(\bar{\psi}\psi)^3 - \frac{1}{4}\gamma_S(\bar{\psi}\psi)^4 - \frac{1}{4}\gamma_V[(\bar{\psi}\gamma_\mu\psi)(\bar{\psi}\gamma^\mu\psi)]^2 \\ &\quad - \frac{1}{2}\delta_S\partial_\nu(\bar{\psi}\psi)\partial^\nu(\bar{\psi}\psi) - \frac{1}{2}\delta_V\partial_\nu(\bar{\psi}\gamma_\mu\psi)\partial^\nu(\bar{\psi}\gamma^\mu\psi) \\ &\quad - \frac{1}{2}\delta_{TV}\partial_\nu(\bar{\psi}\vec{\tau}\gamma_\mu\psi)\partial^\nu(\bar{\psi}\vec{\tau}\gamma^\mu\psi) \\ &\quad - \frac{1}{4}F^{\mu\nu}F_{\mu\nu} - e\frac{1-\tau_3}{2}\bar{\psi}\gamma^\mu\psi A_\mu, \end{aligned} \quad (1)$$

in which the free nucleon term $\mathcal{L}^{\text{free}}$, the four-fermion point-coupling terms $\mathcal{L}^{4\text{f}}$, the higher-order terms \mathcal{L}^{hot} corresponding the medium effects, the gradient terms \mathcal{L}^{der} simulating the

effects of finite range, and the electromagnetic interaction terms \mathcal{L}^{em} are included.

This effective Lagrangian (1) can be rewritten in a rotating frame with a constant rotational frequency ω_x around the x axis [62–64] in order to describe the rotational nuclei via the equation of motion for the nucleons,

$$\hat{h}_0\psi_\mu = (\hat{h}_{\text{s.p.}} + \hat{h}_c)\psi_\mu = \varepsilon_\mu\psi_\mu, \quad (2)$$

with

$$\hat{h}_{\text{s.p.}} = \boldsymbol{\alpha} \cdot (-i\nabla - \mathbf{V}) + \beta(m + S) + V^0, \quad \hat{h}_c = -\omega_x \cdot \hat{J}_x, \quad (3)$$

which is derived from the rotating Lagrangian.

In the equation of motion, $\hat{j}_x = \hat{l}_x + \frac{1}{2}\Sigma_x$ is the x component of the total angular momentum of the nucleon spinors, and ε_μ denotes the single-particle Routhians for nucleons. $S(\mathbf{r})$ and $V^\mu(\mathbf{r})$, which are composed of local densities and currents, are the scalar and the vector fields, respectively.

By solving the equation of motion (2) self-consistently, the total energy of the system in the laboratory is obtained as

$$E_{\text{tot}} = E_{\text{kin}} + E_{\text{int}} + E_{\text{cou}} + E_{\text{c.m.}}, \quad (4)$$

where E_{kin} , E_{int} , E_{cou} , and $E_{\text{c.m.}}$ are the kinetic energy, the interaction energy, the electromagnetic energy, and the center-of-mass (c.m.) correction, respectively.

The Dirac equation (2) can be solved by expanding the nucleon spinors in a complete set of basis. In this work, three-dimensional harmonic oscillator (3DHO) bases with good signature quantum number in Cartesian coordinates [5,65–68] are adopted as follows:

$$\begin{aligned} \Phi_{\xi^+}(\mathbf{r}, s) &= \langle \mathbf{r}, s | \xi \alpha = + \rangle \\ &= \phi_{n_x} \phi_{n_y} \phi_{n_z} \frac{i^{n_y}}{\sqrt{2}} (-1)^{n_z+1} \begin{pmatrix} 1 \\ (-1)^{n_y+n_z} \end{pmatrix}, \end{aligned} \quad (5)$$

$$\begin{aligned} \Phi_{\xi^-}(\mathbf{r}, s) &= \langle \mathbf{r}, s | \xi \alpha = - \rangle \\ &= \phi_{n_x} \phi_{n_y} \phi_{n_z} \frac{i^{n_y}}{\sqrt{2}} \begin{pmatrix} 1 \\ (-1)^{n_y+n_z+1} \end{pmatrix}, \end{aligned} \quad (6)$$

which correspond to the eigenfunctions of the signature operation with the positive ($\alpha = +1/2$) and negative ($\alpha = -1/2$) eigenvalues, respectively. The n_x , n_y , and n_z represent the harmonic oscillator quantum numbers in x , y , and z directions, and ϕ_{n_x} , ϕ_{n_y} and ϕ_{n_z} denote the corresponding eigenstates.

The shell-model-like approach starts from a cranking many-body Hamiltonian including pairing correlations

$$\hat{H} = \hat{H}_0 + \hat{H}_{\text{pair}}, \quad (7)$$

where $\hat{H}_0 = \sum \hat{h}_0$ is the one-body Hamiltonian with the definition of \hat{h}_0 in Eq. (2). The monopole pairing Hamiltonian \hat{H}_{pair} is expressed as

$$\hat{H}_{\text{pair}} = -G \sum_{\substack{\xi \neq \eta \\ \xi, \eta > 0}} \hat{\beta}_\xi^\dagger \hat{\beta}_\xi^\dagger \hat{\beta}_\eta \hat{\beta}_\eta, \quad (8)$$

where the constant number G is the pairing strength, $\bar{\xi}(\bar{\eta})$ labels the time-reversal states of ξ (η), and $\xi \neq \eta$ indicates that the self-scattering for the nucleon pairs is forbidden [44].

The main idea of SLAP is to diagonalize the many-body Hamiltonian (7) in an MPC space with a conserved particle number [23]. One can diagonalize the cranking many-body Hamiltonian (7) in the MPC space constructed from the single-particle states either in the CDFT or in the cranking CDFT.

The single-particle Routhian $\varepsilon_{\mu\alpha}$,

$$\hat{H}_0 = \sum_{\mu\alpha} \varepsilon_{\mu\alpha} \hat{b}_{\mu\alpha}^\dagger \hat{b}_{\mu\alpha}, \quad (9)$$

and the corresponding eigenstate $|\mu\alpha\rangle$,

$$|\mu\alpha\rangle = \sum_{\xi} C_{\mu\xi}(\alpha) |\xi\alpha\rangle. \quad (10)$$

for each level μ with the signature α can be obtained by diagonalizing the one-body Hamiltonian \hat{H}_0 in the basis $|\xi\alpha\rangle$, Eqs. (5) and (6).

Based on the single-particle Routhian $\varepsilon_{\mu\alpha}$ and the corresponding eigenstate $|\mu\alpha\rangle$ (briefly denoted by $|\mu\rangle$), the MPC $|i\rangle$ for an n -particle system can be constructed as [69]

$$|i\rangle = |\mu_1\mu_2\cdots\mu_n\rangle = \hat{b}_{\mu_1}^\dagger \hat{b}_{\mu_2}^\dagger \cdots \hat{b}_{\mu_n}^\dagger |0\rangle. \quad (11)$$

The parity π , signature α , and the corresponding configuration energy for each MPC are determined by the occupied single-particle states.

The eigenstates for the cranking many-body Hamiltonian are obtained by diagonalization in the MPC space,

$$|\Psi\rangle = \sum_i C_i |i\rangle, \quad (12)$$

where C_i is the expansion coefficient.

The occupation probability n_μ for state μ is defined as

$$n_\mu = \sum_i |C_i|^2 P_{i\mu}, \quad P_{i\mu} = \begin{cases} 1, & |i\rangle \text{ contains } |\mu\rangle, \\ 0, & \text{otherwise.} \end{cases} \quad (13)$$

The occupation probabilities will be iterated back into the densities and currents to ensure self-consistency [44].

It is noted that, for the total energy in CDFT (4), the pairing energy due to the pairing correlations should be taken into account, $E_{\text{pair}} = \langle \Psi | \hat{H}_{\text{pair}} | \Psi \rangle$.

For each rotational frequency ω , the expectation values of the angular momentum J_x in the intrinsic frame are given by

$$J_x = \langle \Psi | \hat{J}_x | \Psi \rangle = \sum_i C_i^2 \langle i | \hat{J}_x | i \rangle + \sum_{i,j} C_i C_j \langle i | \hat{J}_x | j \rangle. \quad (14)$$

By means of the semiclassical cranking condition

$$J_x = \langle \Psi | \hat{J}_x | \Psi \rangle = \sqrt{I(I+1)}, \quad (15)$$

one can obtain the angular momentum quantum number I . The kinetic $\mathfrak{I}^{(1)}$ and dynamic $\mathfrak{I}^{(2)}$ moments of inertia then can be calculated by

$$\mathfrak{I}^{(1)} = \frac{J_x}{\omega}, \quad (16)$$

$$\mathfrak{I}^{(2)} = \frac{dJ_x}{d\omega}. \quad (17)$$

The quadrupole moments Q_{20} and Q_{22} are calculated by

$$Q_{20} = \sqrt{\frac{5}{16\pi}} \langle 3z^2 - r^2 \rangle, \quad (18)$$

$$Q_{22} = \sqrt{\frac{15}{32\pi}} \langle x^2 - y^2 \rangle. \quad (19)$$

From the quadrupole moments, the $B(E2)$ transition probabilities can be evaluated by the semiclassical approximation as

$$B(E2) = \frac{3}{8} \left[Q_{20}^p \cos^2 \theta_J + \sqrt{\frac{2}{3}} Q_{22}^p (1 + \sin^2 \theta_J) \right]^2, \quad (20)$$

where Q_{20}^p and Q_{22}^p correspond to the quadrupole moments of protons. θ_J is the angle between the angular momentum vector and the x axis. In this work, only J_x is considered, thus θ_J is zero.

III. NUMERICAL DETAILS

As mentioned in the above section, the equation of motion (2) for the nucleons is solved by expanding the Dirac spinor in the 3DHO bases expressed as Eqs. (5) and (6) with 12 major shells. The convergence of the CDFT-SLAP calculation results with the major shell has been checked by expanding from 8 to 16 major shells. The total energy changes only 0.002% (from -862.3143 MeV to -862.3346 MeV), and the root-mean-square radius of matter changes 0.02% (from 4.4379 to 4.4389 fm) by increasing the major shell from 12 to 14. The multiparticle configuration truncation energies E_c are fixed as 10 MeV for neutrons and 15 MeV for protons, respectively. The corresponding dimensions of MPCs with this cutoff are 1500–2000 for neutrons and around 5000 for protons. In this work, the following pairing strengths sets are adopted: (a) $G_n = G_p = 0$ MeV, (b) $G_n = 0.70$ MeV, $G_p = 0.65$ MeV, (c) $G_n = 1.05$ MeV, $G_p = 0.98$ MeV [50% greater than set (b)], and (d) $G_n = 1.40$ MeV, $G_p = 1.30$ [100% greater than set (b)]. Among them, the CDFT-SLAP calculation with pairing strength set (b) $G_n = 0.70$ MeV, $G_p = 0.65$ MeV can reproduce the experimental even-odd mass differences [44]. In the CDFT-SLAP framework, the parity is a good quantum number. One should specify the parity in the calculation. The protons and neutrons are treated separately in this work. According to the experimental suggestion [59,60], the AMR band is based on the $vh11/2$ band. That means, in the present calculations, the parity of neutrons is negative. The even protons have a positive parity. The signature α equals $-1/2$ (0) for neutrons (protons).

IV. RESULTS AND DISCUSSION

The CDFT-SLAP calculation results show that there are four proton holes below $Z = 50$ in $1g_{9/2,\pm 1/2}$ and $1g_{9/2,\pm 5/2}$ with increasing frequency. The expression $1g_{9/2,\pm 1/2}$ denotes the quantum number nl_{j,m_z} for the single-particle state. In the present calculation results for $\hbar\omega = 0.0$ MeV, the lowest occupied negative parity single-particle state is $1h_{11/2,-11/2}$ with the signature $\alpha = -1/2$. With increasing rotational frequency, the lowest occupied negative parity single-particle

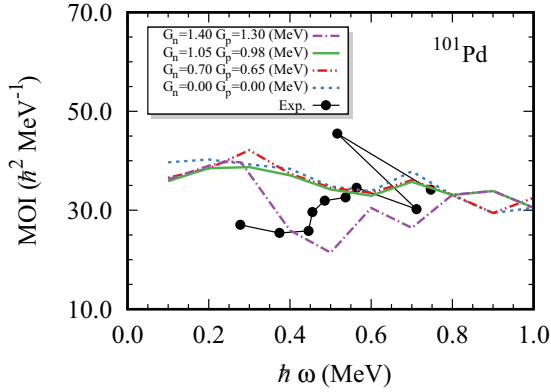


FIG. 1. The experimental (full circle) and calculated kinematic MOIs $\mathfrak{I}^{(1)}$ as a function of rotational frequency $\hbar\omega$ with different pairing strengths: (a) $G_n = G_p = 0$ MeV (blue dashed line), (b) $G_n = 0.70$ MeV, $G_p = 0.65$ MeV (red dash-dot-dot line), (c) $G_n = 1.05$ MeV, $G_p = 0.98$ MeV (green solid line), and (d) $G_n = 1.40$ MeV, $G_p = 1.30$ MeV (purple dash-dot line) for ^{101}Pd . The experimental data are taken from Ref. [60].

state is $1h_{11/2,-5/2}$ instead of $1h_{11/2,-11/2}$ when the rotational frequency $\hbar\omega$ is higher than 0.1 MeV. In Refs. [59,60], a semiclassical particle-rotor model described the AMR band in ^{101}Pd with fixed configurations $(\pi g_{9/2}^{-4}) \otimes (\nu h_{11/2})$ and $(\pi g_{9/2}^{-4}) \otimes (\nu h_{11/2} g_{7/2}^2)$ for low rotational frequency and high rotational frequency, respectively. However, in the CDFT-SLAP calculation, without any arbitrarily fixed configurations, the full self-consistent CDFT-SLAP model can provide similar configurations for ^{101}Pd .

Figure 1 shows the experimental (full circle) and calculated kinematic MOIs $\mathfrak{I}^{(1)}$ as a function of rotational frequency $\hbar\omega$ with different pairing strengths: (a) $G_n = G_p = 0$ MeV (blue dashed line), (b) $G_n = 0.70$ MeV, $G_p = 0.65$ MeV (red dash-dot-dot line), (c) $G_n = 1.05$ MeV, $G_p = 0.98$ MeV (green solid line), and (d) $G_n = 1.40$ MeV, $G_p = 1.30$ MeV (purple dash-dot line) for ^{101}Pd . The experimental data are taken from Ref. [60]. In this work, the experimental rotational frequency is extracted as in Ref. [16],

$$\hbar\omega_{\text{exp.}} = \frac{1}{2}E_\gamma(I \rightarrow I-2), \quad (21)$$

where I is the quantum number of the angular momentum. It can be found that the calculated MOI $\mathfrak{I}^{(1)}$ without pairing, i.e. with pairing strength (a) $G_n = G_p = 0$ MeV, decreases very slowly before $\hbar\omega = 0.6$ MeV, and increases linearly with frequency $\hbar\omega$ from 0.6 to 0.7 MeV. With the frequency $\hbar\omega$ between 0.7 and 0.8 MeV, the MOI $\mathfrak{I}^{(1)}$ drops linearly again. Similar behavior can be seen for the calculated MOI $\mathfrak{I}^{(1)}$ with pairing strengths (b) $G_n = 0.70$ MeV, $G_p = 0.65$ MeV and (c) $G_n = 1.05$ MeV, $G_p = 0.98$ MeV. The stronger pairing force with (d) $G_n = 1.40$ MeV, $G_p = 1.30$ MeV leads to rapid decrease of $\mathfrak{I}^{(1)}$ before $\hbar\omega = 0.5$ MeV and advanced staggering. The experimental up-bending with the rotational frequency $\hbar\omega$ between 0.4 and 0.5 MeV, which is interpreted as alignments of two $g_{7/2}$ quasineutrons in Refs [59,60], is reproduced at different frequency regions in this work. The calculated MOI $\mathfrak{I}^{(1)}$ increases rapidly with $\hbar\omega$ from 0.6 to

0.7 MeV for pairing strengths (a) $G_n = G_p = 0$ MeV, (b) $G_n = 0.70$ MeV, $G_p = 0.65$ MeV, and (c) $G_n = 1.05$ MeV, $G_p = 0.98$ MeV. It rises up from 0.5 to 0.6 MeV for (d) $G_n = 1.40$ MeV, $G_p = 1.30$ MeV. Meanwhile, the calculated back-bending occurs after $\hbar\omega = 0.8$ MeV for pairing strength sets (a), (b), and (c), and beyond 0.7 MeV for pairing strength set (d). Generally speaking, the up-bending and back-bending have been postponed compared to the experiment. The stronger pairing force can accelerate their occurrence.

In addition, it can be seen that the pairing effects on the moment of inertia are small at the lowest rotational frequency. This can be understood by the single-particle Routhians. The calculated single-particle Routhians for both neutrons and protons as functions of the rotational frequency show that the $(1g_{9/2,1/2})$ and $(1g_{9/2,-1/2})$ orbitals of the protons degenerate at low frequency, as well as $(1g_{9/2,5/2})$ and $(1g_{9/2,-5/2})$ of the protons. The most distinguished feature is that there are large energy gaps (~ 2 MeV) among $(1g_{9/2,\pm 1/2})$, $(1g_{9/2,\pm 5/2})$, and $(1g_{9/2,\pm 7/2})$ for the ^{101}Pd proton at low frequency. Since the AMR in ^{101}Pd is explained by the alignment of four proton holes in the $1g_{9/2}$ orbital, the pairing effects are very small at low frequency due to these large gaps. In other words, the four proton holes appear at lowest frequency and do not change very much with the pairing due to these large gaps. This is shown in Fig. 5, in which the occupation number of proton $1g_{9/2}$ do not change very much with different pairing strengths. The small pairing effects can also be understood by Fig. 4, where the total angular momentum does not change very much with a different pairing. Since the MOI $\mathfrak{I}^{(1)}$ is calculated with the J_x divided by the rotational frequency, the moment of inertia does not change much with the pairing correlation.

For the same reason, the four proton holes start to appear and contribute to the total angular momentum at the lowest frequency. As a result, the total angular momentum J_x of the proton at the lower frequency is not small. Thus the calculated moments of inertia (except with the largest pairing strength) are much larger than the experimental values when the rotational frequency is less than 0.5 MeV. By increasing the pairing strength, e.g., using the largest pairing strength set, there are significant possibilities of scattering particles in other orbitals to $1g_{9/2}$. This is not conducive to the formation of four proton holes. The total angular momentum J_x of the proton at the lower frequency is small, and the MOI $\mathfrak{I}^{(1)}$ is small.

The experimental (full circles) and calculated $B(E2)$ values for ^{101}Pd as a function of the rotational frequency with different pairing strengths are shown in Fig. 2, for (a) $G_n = G_p = 0$ MeV (blue dashed line), (b) $G_n = 0.70$ MeV, $G_p = 0.65$ MeV (red dash-dot-dot line), (c) $G_n = 1.05$ MeV, $G_p = 0.98$ MeV (green solid line), and (d) $G_n = 1.40$ MeV, $G_p = 1.30$ MeV (purple dash-dot line). The inset shows the experimental and calculated $B(E2)$ with pairing strengths above as a function of total angular momentum quantum number I . The data are taken from Ref. [60]. All the calculation results except that with pairing strength (d) $G_n = 1.40$ MeV, $G_p = 1.30$ MeV can reproduce the experimental tendency of $B(E2)$ for ^{101}Pd very well. By enhancing the pairing correlation, the $B(E2)$ values decrease systematically. The calculated $B(E2)$

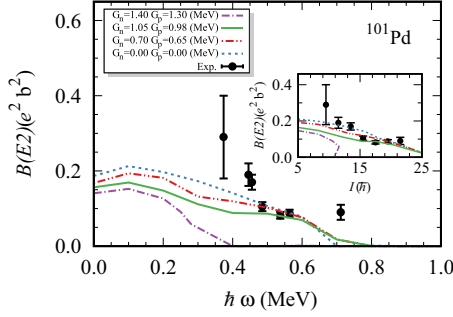


FIG. 2. The experimental (full circles) and calculated $B(E2)$ values as a function of the rotational frequency with different pairing strengths: (a) $G_n = G_p = 0$ MeV (blue dashed line), (b) $G_n = 0.70$ MeV, $G_p = 0.65$ MeV (red dash-dot-dot line), (c) $G_n = 1.05$ MeV, $G_p = 0.98$ MeV (green solid line), and (d) $G_n = 1.40$ MeV, $G_p = 1.30$ MeV (purple dash-dot line) for ^{101}Pd . The inset shows the $B(E2)$ values as a function of total angular momentum quantum number I . The data are taken from Ref. [60].

with the strongest pairing strength drops very rapidly and reaches zero at $\hbar\omega = 0.4$ MeV. It can be also found that the calculated $B(E2)$ values with pairing strength sets (a), (b), and (c) decrease obviously from $\hbar\omega = 0.6$ MeV to 0.7 MeV. This corresponds to the abrupt change of MOI $\mathfrak{S}^{(1)}$ at the same frequency range. According to above discussion, the cranking CDFT-SLAP calculations could provide a reasonable description of the experimental $B(E2)$ values for ^{101}Pd , which is one of the most characteristic features of AMR, i.e., decreasing $B(E2)$ values with rotation.

In the calculation in the inset figure, the quantal corrections have been taken into account [70]. It can be also seen that all CDFT-SLAP calculations with three sets of pairing strengths can describe the property of $B(E2)$ very well with respect to total spin. More precisely, the calculations with weak pairing forces (a) $G = 0$ and (b) $G_n = 0.7$ MeV, $G_p = 0.65$ MeV provide better description of $B(E2)$ for the rotation with the low total spin, and a stronger pairing strength set (c) $G_n = 1.05$ MeV, $G_p = 0.98$ reproduces the high spin rotation well. This could be explained by the fact that (1) the pairing effects reduce the deformation of ^{101}Pd at low frequency and (2) the effects of pairing force on high frequencies are small.

Figure 3 shows the experimental (full circles) and calculated total angular momentum quantum numbers as a function of the rotational frequency with different pairing strengths: (a) $G_n = G_p = 0$ MeV (blue dashed line), (b) $G_n = 0.70$ MeV, $G_p = 0.65$ MeV (red dash-dot-dot line), (c) $G_n = 1.05$ MeV, $G_p = 0.98$ MeV (green solid line), and (d) $G_n = 1.40$ MeV, $G_p = 1.30$ MeV (purple dash-dot line) for ^{101}Pd . The data are taken from Ref. [60]. All the calculations can provide a good description of the increasing tendency for the experimental total spin. The total spins with pairing strengths (a) $G_n = G_p = 0$ MeV, (b) $G_n = 0.70$ MeV, $G_p = 0.65$ MeV, and (c) $G_n = 1.05$ MeV, $G_p = 0.98$ MeV demonstrate similar behavior before $\hbar\omega = 0.8$ MeV. Two turning points can also be observed at $\hbar\omega = 0.6$ and 0.7 MeV. However, in analogy to the calculated MOI $\mathfrak{S}^{(1)}$ shown in Fig. 1, the calculated total spin with a stronger pairing correlation shows a step-like

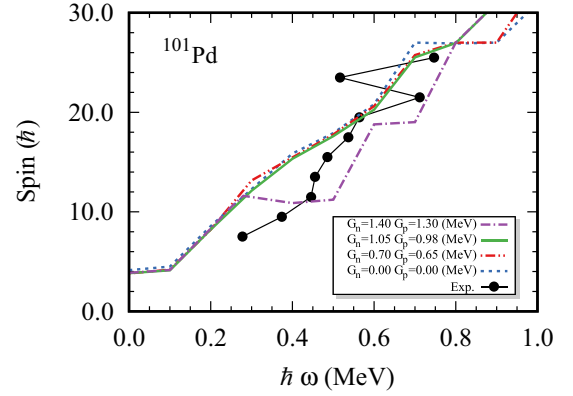


FIG. 3. The experimental (full circles) and calculated total angular momentum quantum number as a function of the rotational frequency with different pairing strengths: (a) $G_n = G_p = 0$ MeV (blue dashed line), (b) $G_n = 0.70$ MeV, $G_p = 0.65$ MeV (red dash-dot-dot line), (c) $G_n = 1.05$ MeV, $G_p = 0.98$ MeV (green solid line), and (d) $G_n = 1.40$ MeV, $G_p = 1.30$ MeV (purple dash-dot line) for ^{101}Pd . The data are taken from Ref. [60].

growth, which is closer to the experimental alignment starting from $\hbar\omega = 0.4$ MeV and the back-bending at $\hbar\omega = 0.7$ MeV.

The experimental (full circles) and calculated expectation values of angular momentum along the x axis, J_x , are shown in Fig. 4 as functions of the rotational frequency $\hbar\omega$ with different pairing strengths: (a) $G_n = G_p = 0$ MeV (top left panel), (b) $G_n = 0.70$ MeV, $G_p = 0.65$ MeV (top right panel), (c) $G_n = 1.05$ MeV, $G_p = 0.98$ MeV (bottom left panel), and (d) $G_n = 1.40$ MeV, $G_p = 1.30$ MeV (bottom right) for neutrons (blue dash-dot lines), protons (red dashed lines), and total contribution (green solid lines). Without pairing, the expectation value of angular momentum J_x of the neutron increases

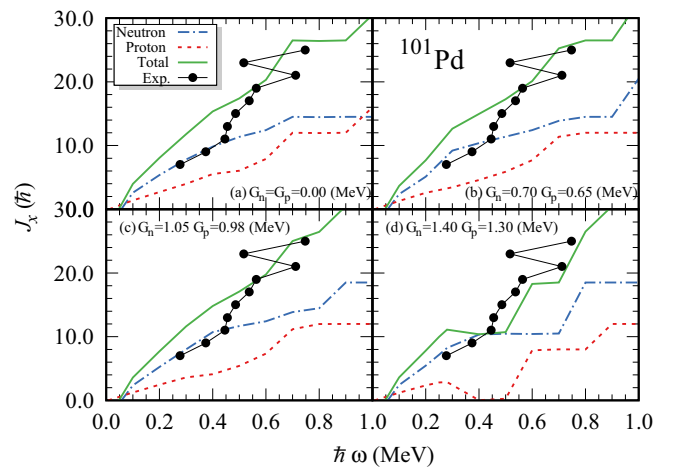


FIG. 4. The experimental (full circles) and calculated expectation values of angular momentum along the x axis, J_x , as functions of $\hbar\omega$ with different pairing strengths: (a) $G_n = G_p = 0$ MeV, (b) $G_n = 0.70$ MeV, $G_p = 0.65$ MeV, (c) $G_n = 1.05$ MeV, $G_p = 0.98$ MeV, and (d) $G_n = 1.40$ MeV, $G_p = 1.30$ MeV for neutrons (blue dash-dot lines), protons (red dashed lines), and total contribution (green solid lines) for ^{101}Pd . The data are taken from Ref. [60].

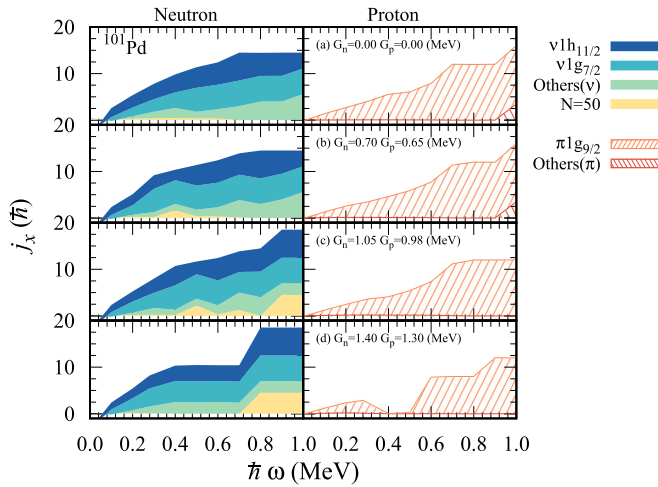


FIG. 5. Angular momentum alignment j_x of neutrons (left column) and protons (right column) for ^{101}Pd as functions of rotational frequency $\hbar\omega$ with different pairing strengths: (a) $G_n = G_p = 0$ MeV, (b) $G_n = 0.70$ MeV, $G_p = 0.65$ MeV, (c) $G_n = 1.05$ MeV, $G_p = 0.98$ MeV, and (d) $G_n = 1.40$ MeV, $G_p = 1.30$ MeV. The angular momentum alignment composition of $1h_{11/2}$, $1g_{7/2}$, $N = 50$ core ($\hbar\omega = 0$ MeV), and other orbits of neutrons is illustrated by different colors, as is the composition of $1g_{9/2}$ and other orbits of protons.

almost linearly up to $\hbar\omega = 0.7$ MeV, and stays constant after that. The angular momentum J_x of the proton increases with different rates from $\hbar\omega = 0.6$ to 0.7 MeV and $\hbar\omega > 0.9$ MeV. Between 0.7 and 0.9 MeV, the J_x of the proton is almost a constant number. The properties of calculated angular momentum expectation value J_x with pairing strengths (b) and (c) are very similar for neutrons, as well as for protons. The significant growth of J_x for the neutron happens at high rotational frequency $\hbar\omega > 0.8$ MeV. However, the remarkable change for proton angular momentum appears between $\hbar\omega = 0.6$ and 0.7 MeV, which is closer to the experimental alignment of angular momentum at $\hbar\omega = 0.45\text{--}0.6$ MeV. The conclusion that the experimental alignment of angular momentum mainly comes from the contribution of the proton can be seen clearly in Fig. 4(d), which is obtained by the calculation with a stronger pairing force. The J_x of the neutron stays constant from $\hbar\omega = 0.4$ to 0.7 MeV and beyond 0.8 MeV. It increases linearly between $\hbar\omega = 0.7$ and 0.8 MeV. The present results are different from those obtained in Refs. [59,60], where the increase of the angular momentum alignment is assumed to be obtained from the alignment of one $g_{7/2}$ neutron pair. In this work, the contributions from neutrons are equally as important as those from protons to the total angular momentum. However, the alignment of angular momentum corresponding to the experimental up-bending at $\hbar\omega = 0.45$ MeV comes mainly from the proton, which is supported by the PNC-CSM calculation in Ref. [61]. Moreover, the weaker pairing force leads to the continuous and smooth change of the angular momentum, compared with the step-like and abrupt change caused by the stronger pairing correlation.

It is necessary to investigate the contribution to the angular momentum in terms of single-particle orbitals. In Fig. 5,

the angular momentum alignment j_x of neutrons (left column) and protons (right column) for ^{101}Pd is shown as functions of rotational frequency $\hbar\omega$ with different pairing strengths: (a) $G_n = G_p = 0$ MeV, (b) $G_n = 0.70$ MeV, $G_p = 0.65$ MeV, (c) $G_n = 1.05$ MeV, $G_p = 0.98$ MeV, and (d) $G_n = 1.40$ MeV, $G_p = 1.30$ MeV. The angular momentum alignment composition of single-particle orbitals $1h_{11/2}$, $1g_{7/2}$, $N = 50$ core ($\hbar\omega = 0$ MeV), and other orbitals of the neutron is illustrated by different colors, as is the composition of $1g_{9/2}$ and other orbits of the proton. It should be noted that these orbitals are labeled by their main component. It can be seen that the $1h_{11/2}$ and $1g_{7/2}$ orbitals make almost the same contribution and are dominant to the angular momentum of the neutron. With weak pairing force, like strength sets (a) and (b), the orbits below $N = 50$ contribute nearly zero to the neutron angular momentum. The remaining contribution of the angular momentum comes from $2d_{5/2,3/2}$ and $3s_{1/2}$ orbits, which are labeled as others (ν) in this figure. With increasing pairing strength, as shown in the third and fourth panels, the orbits below $N = 50$ become important at a high rotational frequency. In the case of the proton, the $1g_{9/2}$ orbit plays an absolutely dominant role to J_x . Obviously, this orbit makes the alignment at the rotational frequency from 0.6 to 0.7 MeV in the first, second, and third panels, and the alignment from $\hbar\omega = 0.5$ to 0.6 MeV and from 0.8 to 0.9 MeV in the fourth panel. However, the alignment of proton angular momentum beyond 0.9 MeV comes from other orbits instead of $1g_{9/2}$ orbit.

In order to understand the contribution to the angular momentum from different single-particle orbitals, it is interesting to analyze the occupation property for these orbitals. The occupation numbers of single-particle orbitals (a) $\nu 1h_{11/2}$, (b) $\nu 1g_{7/2}$ for neutrons, and (c) $\pi 1g_{9/2}$ for protons of ^{101}Pd as functions of rotational frequency $\hbar\omega$ are shown in Fig. 6 with different pairing strengths: (a) $G_n = G_p = 0$ MeV (blue dashed lines), (b) $G_n = 0.70$ MeV, $G_p = 0.65$ MeV (red dash-dot lines), (c) $G_n = 1.05$ MeV, $G_p = 0.98$ MeV (green solid lines), and (d) $G_n = 1.40$ MeV, $G_p = 1.30$ MeV (purple dash-dot lines). It can be found that the occupation number of $1h_{11/2}$ decreases with the rotation and reaches 1. Moreover, the stronger pairing leads to bigger occupation number since the pairing could scatter the paired particles from other orbits to $1h_{11/2}$. Although the occupation number is decreasing, the component of $1h_{11/2}$ in this orbit is increasing and become a pure $1h_{11/2}$ orbit at high frequency. The occupation numbers of $\pi 1g_{7/2}$ oscillate around 2 as a function of $\hbar\omega$. This can be understood by the strong mixture among $1g_{7/2}$ and orbits nearby. This accords with the fluctuation of the contribution to the angular momentum of this orbit in Fig. 5. In the case of the proton $1g_{9/2}$, decreasing of the occupation number with the rotation means the formation of four proton holes. Meanwhile, the purity of $1g_{9/2}$ is increasing. For example, the average component of $1g_{9/2}$ in this orbit increases from 60%, 93%, to 98% at $\hbar\omega = 0.1, 0.5$, and 0.9 MeV, respectively, with pairing strength (d) $G_n = 1.40$ MeV, $G_p = 1.30$ MeV. This can explain why the contribution to angular momentum increases while the occupation number for single-particle orbitals decreases. It is due to the situation that four proton holes in $1g_{9/2}$ have evolved with the increase of frequency

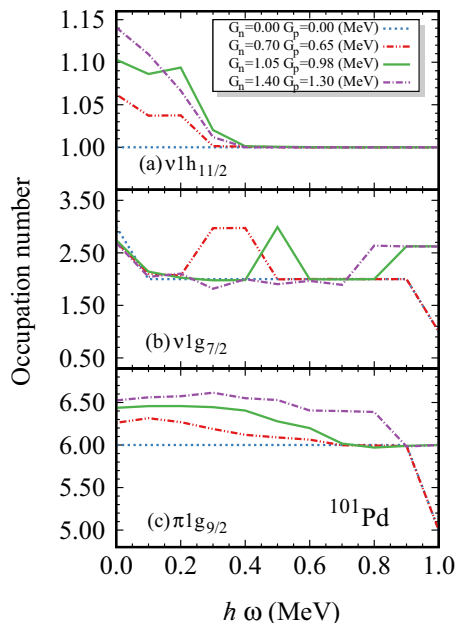


FIG. 6. Occupation numbers of single-particle orbits (a) $\nu 1h_{11/2}$, (b) $\nu 1g_{7/2}$ for neutrons, and (c) $\pi 1g_{9/2}$ for protons of ^{101}Pd as functions of rotational frequency $\hbar\omega$ with different pairing strengths: (a) $G_n = G_p = 0$ MeV (blue dashed lines), (b) $G_n = 0.70$ MeV, $G_p = 0.65$ MeV (red dash-dot-dot lines), (c) $G_n = 1.05$ MeV, $G_p = 0.98$ MeV (green solid lines), and (d) $G_n = 1.40$ MeV, $G_p = 1.30$ MeV (purple dash-dot lines).

and contribute to the total angular momentum. This pattern is defined as the two-shears-like mechanism in AMR.

V. SUMMARY

In this work, the antimagnetic rotation band $\nu h_{11/2}$ in ^{101}Pd is investigated by the cranking covariant density functional

theory with a shell-model-like approach to treat the pairing correlations, in which the particle number is conserved strictly and the blocking effects are taken into account exactly. Four sets of pairing strength are adopted in the present calculation in order to investigate the effect of pairing to the AMR. The tendencies of experimental moments of inertia, reduced $B(E2)$ transition probabilities, and the spin are well reproduced by the cranking CDFT-SLAP calculations with suitable pairing strengths. The discrepancy is also discussed in terms of the single-particle Routhians, the occupation numbers, and the component of angular momentum. In the competition of pairing correlations and rotations, the stronger pairing force will lead to drastic and step-like changes of these quantities while the weak pairing only gives rise to mild and gradual modifications. By investigating the $\hbar\omega$ dependence for the contributions of orbitals to the total angular momentum alignment and the occupation numbers around the Fermi surface, the up-bending mechanism of AMR band $\nu h_{11/2}$ in ^{101}Pd is understood clearly. This up-bending with $\hbar\omega = 0.45$ MeV mainly triggered by the proton $1g_{9/2}$ orbital—more precisely, by four proton holes in this orbital—while the neutron $1h_{11/2}$ and $1g_{7/2}$ orbitals only contribute to the homogeneous increase of total angular momentum. Moreover, it is found that the proton angular momentum alignment, which mainly comes from the rearrangement of proton occupations in $1g_{9/2}$ orbitals and the increasing shears-like mechanism.

ACKNOWLEDGMENTS

This work was supported by the National Natural Science Foundation of China (Grant No. 11775099). Helpful discussions with Z. Shi, Z. H. Zhang, and B. W. Xiong are gratefully acknowledged. The author would like to thank J. Meng and P. W. Zhao for inspiration.

- [1] S. Frauendorf, in *Proceedings of the Workshop on Gamma-sphere Physics, Berkeley*, edited by M. A. Deleplanque, I. Y. Lee, and A. O. Macchiavelli (World Scientific, Singapore, 1995), p. 272.
- [2] S. Frauendorf, *Rev. Mod. Phys.* **73**, 463 (2001).
- [3] R. M. Clark and A. O. Macchiavelli, *Annu. Rev. Nucl. Part. Sci.* **50**, 1 (2000).
- [4] S. Frauendorf, *Nucl. Phys. A* **677**, 115 (2000).
- [5] J. Peng, J. Meng, P. Ring, and S. Q. Zhang, *Phys. Rev. C* **78**, 024313 (2008).
- [6] P. W. Zhao, S. Q. Zhang, J. Peng, H. Z. Liang, P. Ring, and J. Meng, *Phys. Lett. B* **699**, 181 (2011).
- [7] A. J. Simons, R. Wadsworth, D. G. Jenkins, R. M. Clark, M. Cromaz, M. A. Deleplanque, R. M. Diamond, P. Fallon, G. J. Lane, I. Y. Lee, A. O. Macchiavelli, F. S. Stephens, C. E. Svensson, K. Vetter, D. Ward, and S. Frauendorf, *Phys. Rev. Lett.* **91**, 162501 (2003).
- [8] A. J. Simons, R. Wadsworth, D. G. Jenkins, R. M. Clark, M. Cromaz, M. A. Deleplanque, R. M. Diamond, P. Fallon, G. J. Lane, I. Y. Lee, A. O. Macchiavelli, F. S. Stephens, C. E. Svensson, K. Vetter, D. Ward, S. Frauendorf, and Y. Gu, *Phys. Rev. C* **72**, 024318 (2005).
- [9] S. Zhu, U. Garg, A. V. Afanasjev, S. Frauendorf, B. Khararaja, S. S. Ghugre, S. N. Chintalapudi, R. V. F. Janssens, M. P. Carpenter, F. G. Kondev, and T. Lauritsen, *Phys. Rev. C* **64**, 041302 (2001).
- [10] C. J. Chiara, S. J. Asztalos, B. Busse, R. M. Clark, M. Cromaz, M. A. Deleplanque, R. M. Diamond, P. Fallon, D. B. Fossan, D. G. Jenkins, S. Juutinen, N. S. Kelsall, R. Krücken, G. J. Lane, I. Y. Lee, A. O. Macchiavelli, R. W. MacLeod, G. Schmid, J. M. Sears, J. F. Smith, F. S. Stephens, K. Vetter, R. Wadsworth, and S. Frauendorf, *Phys. Rev. C* **61**, 034318 (2000).
- [11] P. Ring, *Prog. Part. Nucl. Phys.* **37**, 193 (1996).
- [12] J. Meng, H. Toki, S. Zhou, S. Zhang, W. Long, and L. Geng, *Prog. Part. Nucl. Phys.* **57**, 470 (2006).
- [13] J. Meng, *Relativistic Density Functional for Nuclear Structure* (World Scientific, Singapore, 2015).
- [14] W. H. Long, J. Meng, N. Van Giai, and S. G. Zhou, *Phys. Rev. C* **69**, 034319 (2004).
- [15] P. W. Zhao, J. Peng, H. Z. Liang, P. Ring, and J. Meng, *Phys. Rev. Lett.* **107**, 122501 (2011).
- [16] P. W. Zhao, J. Peng, H. Z. Liang, P. Ring, and J. Meng, *Phys. Rev. C* **85**, 054310 (2012).

- [17] L. Liu and P. Zhao, *Sci. China Phys. Mech. Astron.* **55**, 2420 (2012).
- [18] J. Peng and P. W. Zhao, *Phys. Rev. C* **91**, 044329 (2015).
- [19] P. W. Zhao, Z. P. Li, J. M. Yao, and J. Meng, *Phys. Rev. C* **82**, 054319 (2010).
- [20] J. Meng and P. Zhao, *Phys. Scr.* **91**, 053008 (2016).
- [21] P. W. Zhao, N. Itagaki, and J. Meng, *Phys. Rev. Lett.* **115**, 022501 (2015).
- [22] P. W. Zhao, S. Q. Zhang, and J. Meng, *Phys. Rev. C* **92**, 034319 (2015).
- [23] J. Y. Zeng and T. S. Cheng, *Nucl. Phys. A* **405**, 1 (1983).
- [24] H. Molique and J. Dudek, *Phys. Rev. C* **56**, 1795 (1997).
- [25] B. R. Mottelson and J. G. Valatin, *Phys. Rev. Lett.* **5**, 511 (1960).
- [26] J. Dudek, B. Herskind, W. Nazarewicz, Z. Szymanski, and T. R. Werner, *Phys. Rev. C* **38**, 940 (1988).
- [27] C. S. Wu and J. Y. Zeng, *Phys. Rev. C* **39**, 666 (1989).
- [28] N. Pillet, P. Quentin, and J. Libert, *Nucl. Phys. A* **697**, 141 (2002).
- [29] X. M. Fu, F. R. Xu, J. C. Pei, C. F. Jiao, Y. Shi, Z. H. Zhang, and Y. A. Lei, *Phys. Rev. C* **87**, 044319 (2013).
- [30] X. Fu, C. Jiao, F. Xu, and Z. Zhang, *Sci. China-Phys. Mech. Astron.* **56**, 1423 (2013).
- [31] W. Y. Liang, C. F. Jiao, Q. Wu, X. M. Fu, and F. R. Xu, *Phys. Rev. C* **92**, 064325 (2015).
- [32] J. Y. Zeng, Y. A. Lei, T. H. Jin, and Z. J. Zhao, *Phys. Rev. C* **50**, 746 (1994).
- [33] S. X. Liu, J. Y. Zeng, and E. G. Zhao, *Phys. Rev. C* **66**, 024320 (2002).
- [34] X. T. He, S. X. Liu, S. Y. Yu, J. Y. Zeng, and E. G. Zhao, *Eur. Phys. J. A* **23**, 217 (2005).
- [35] X. Wu, Z. H. Zhang, J. Y. Zeng, and Y. A. Lei, *Phys. Rev. C* **83**, 034323 (2011).
- [36] S. Liu, J. Zeng, and L. Yu, *Nucl. Phys. A* **735**, 77 (2004).
- [37] Z. Zhang, X. Wu, Y. Lei, and J. Zeng, *Nucl. Phys. A* **816**, 19 (2009).
- [38] Z. H. Zhang, Y. A. Lei, and J. Y. Zeng, *Phys. Rev. C* **80**, 034313 (2009).
- [39] Z.-H. Zhang, *Nucl. Phys. A* **949**, 22 (2016).
- [40] X.-T. He, Z.-Z. Ren, S.-X. Liu, and E.-G. Zhao, *Nucl. Phys. A* **817**, 45 (2009).
- [41] Z.-H. Zhang, J.-Y. Zeng, E.-G. Zhao, and S.-G. Zhou, *Phys. Rev. C* **83**, 011304 (2011).
- [42] Z.-H. Zhang, X.-T. He, J.-Y. Zeng, E.-G. Zhao, and S.-G. Zhou, *Phys. Rev. C* **85**, 014324 (2012).
- [43] Z.-H. Zhang, J. Meng, E.-G. Zhao, and S.-G. Zhou, *Phys. Rev. C* **87**, 054308 (2013).
- [44] J. Meng, J. Guo, L. Liu, and S. Zhang, *Front. Phys. China* **1**, 38 (2006).
- [45] L. Liu, J. Meng, and S.-Q. Zhang, *Chin. Phys. C* **30**, 299 (2006).
- [46] P. W. Wang, H. Chen, J. X. Li, L. Liu, and J. Meng, *Chin. Phys. C* **30**, 94 (2006).
- [47] L. Liu, P. W. Wang, H. Chen, and J. Meng, *Chin. Phys. C* **30**, 227 (2006).
- [48] L. Liu and P.-W. Zhao, *Chin. Phys. C* **36**, 818 (2012).
- [49] L. Liu and P.-W. Zhao, *Chin. Phys. C* **38**, 074103 (2014).
- [50] M.-J. Cheng, L. Liu, and Y.-X. Zhang, *Chin. Phys. C* **39**, 104102 (2015).
- [51] L. Liu, Z.-H. Zhang, and P.-W. Zhao, *Phys. Rev. C* **92**, 044304 (2015).
- [52] Z. Shi, Z. H. Zhang, Q. B. Chen, S. Q. Zhang, and J. Meng, *Phys. Rev. C* **97**, 034317 (2018).
- [53] D. Choudhury, A. K. Jain, M. Patial, N. Gupta, P. Arumugam, A. Dhal, R. K. Sinha, L. Chaturvedi, P. K. Joshi, T. Trivedi, R. Palit, S. Kumar, R. Garg, S. Mandal, D. Negi, G. Mohanto, S. Muralithar, R. P. Singh, N. Madhavan, R. K. Bhowmik, and S. C. Pancholi, *Phys. Rev. C* **82**, 061308 (2010).
- [54] P. Datta, S. Chattopadhyay, S. Bhattacharya, T. K. Ghosh, A. Goswami, S. Pal, M. Saha Sarkar, H. C. Jain, P. K. Joshi, R. K. Bhowmik, R. Kumar, N. Madhaban, S. Muralithar, P. V. M. Rao, and R. P. Singh, *Phys. Rev. C* **71**, 041305 (2005).
- [55] S. Roy, S. Chattopadhyay, P. Datta, S. Pal, S. Bhattacharya, R. Bhowmik, A. Goswami, H. Jain, R. Kumar, S. Muralithar, D. Negi, R. Palit, and R. Singh, *Phys. Lett. B* **694**, 322 (2011).
- [56] D. Choudhury, A. K. Jain, G. A. Kumar, S. Kumar, S. Singh, P. Singh, M. Sainath, T. Trivedi, J. Sethi, S. Saha, S. K. Jadav, B. S. Naidu, R. Palit, H. C. Jain, L. Chaturvedi, and S. C. Pancholi, *Phys. Rev. C* **87**, 034304 (2013).
- [57] M. Sugawara, Y. Toh, M. Oshima, M. Koizumi, A. Osa, A. Kimura, Y. Hatsukawa, J. Goto, H. Kusakari, T. Morikawa, Y. H. Zhang, X. H. Zhou, Y. X. Guo, and M. L. Liu, *Phys. Rev. C* **79**, 064321 (2009).
- [58] X. W. Li, J. Li, J. B. Lu, K. Y. Ma, Y. H. Wu, L. H. Zhu, C. Y. He, X. Q. Li, Y. Zheng, G. S. Li, X. G. Wu, Y. J. Ma, and Y. Z. Liu, *Phys. Rev. C* **86**, 057305 (2012).
- [59] M. Sugawara, T. Hayakawa, M. Oshima, Y. Toh, A. Osa, M. Matsuda, T. Shizuma, Y. Hatsukawa, H. Kusakari, T. Morikawa, Z. G. Gan, and T. Czosnyka, *Phys. Rev. C* **86**, 034326 (2012).
- [60] M. Sugawara, T. Hayakawa, M. Oshima, Y. Toh, A. Osa, M. Matsuda, T. Shizuma, Y. Hatsukawa, H. Kusakari, T. Morikawa, Z. G. Gan, and T. Czosnyka, *Phys. Rev. C* **92**, 024309 (2015).
- [61] Z.-H. Zhang, *Phys. Rev. C* **94**, 034305 (2016).
- [62] W. Koepf and P. Ring, *Nucl. Phys. A* **493**, 61 (1989).
- [63] J. König and P. Ring, *Phys. Rev. Lett.* **71**, 3079 (1993).
- [64] K. Kaneko, M. Nakano, and M. Matsuzaki, *Phys. Lett. B* **317**, 261 (1993).
- [65] W. Koepf and P. Ring, *Phys. Lett. B* **212**, 397 (1988).
- [66] J. Dobaczewski and J. Dudek, *Comput. Phys. Commun.* **102**, 166 (1997).
- [67] J. M. Yao, H. Chen, and J. Meng, *Phys. Rev. C* **74**, 024307 (2006).
- [68] T. Nikšić, Z. P. Li, D. Vretenar, L. Próchniak, J. Meng, and P. Ring, *Phys. Rev. C* **79**, 034303 (2009).
- [69] J. Y. Zeng, T. H. Jin, and Z. J. Zhao, *Phys. Rev. C* **50**, 1388 (1994).
- [70] S. Frauendorf and J. Meng, *Z. Phys. A* **356**, 263 (1996).